

# Feedback Control of a Single-Tail Bioinspired 59-mg Swimmer

Conor K. Trygstad, Cody R. Longwell, Francisco M. F. R. Gonçalves, Elijah K. Blankenship,  
and Néstor O. Pérez-Arancibia

**Abstract**—We present an evolved steerable version of the single-tail *Fish-&-Ribbon-Inspired Small Swimming Harmonic roBot* (FRISSHBot), a 59-mg biologically inspired swimmer, which is driven by a new *shape-memory alloy* (SMA)-based bimorph actuator. The new FRISSHBot is controllable in the *two-dimensional* (2D) space, which enabled the first demonstration of feedback-controlled trajectory tracking of a single-tail aquatic robot with onboard actuation at the subgram scale. These new capabilities are the result of a physics-informed design with an enlarged head and shortened tail relative to those of the original platform. Enhanced by its design, this new platform achieves forward swimming speeds of up to 13.6 mm/s (0.38 BI/s), which is over four times that of the original platform. Furthermore, when following 2D references in closed loop, the tested FRISSHBot prototype attains forward swimming speeds of up to 9.1 mm/s, *root-mean-square* (RMS) tracking errors as low as 2.6 mm, turning rates of up to 13.1 °/s, and turning radii as small as 10 mm.

## I. INTRODUCTION

The recent development of numerous mm-to-cm-scale aquatic robots [1]–[21]—with varying levels of performance and efficiency—indicates great interest and substantial progress toward the creation of small-scale autonomous swimmers and, foreseeably, swarms of microswimmers capable of assisting humans with complex tasks in real-world scenarios. Small swimmers have the potential to bring unique capabilities for aquatic applications where maneuvering in confined spaces is required; for example, the inspection of water distribution systems, in which pipe diameters can be as small as 50 and 100 mm for residential and commercial bypass lines, respectively [22]. Additionally, many cm-to-dm-scale fish-inspired and snake-inspired swimmers have been recently reported [23]–[28]. However, the scaling of those prototypes down to the mm-scale has yet to be accomplished.

A gamut of propulsion mechanisms has been used to drive the small-scale aquatic robots mentioned here, including flapping tails and fins [1]–[10], jets [11], [12], and pads and skates for surface crawling or skating [13]–[20]. We envision the development of insect-scale *autonomous underwater vehicles* (AUVs) capable of operating robustly over a wide range of water depths. Flapping tails and jets are propulsion mechanisms that translate adequately to underwater environments, whereas crawling methods based on leveraging the surface tension of water do not. However, it has been reported that the efficiency of jet-based propulsion is two to three times lower than that of undulatory propulsion [29], which suggests that designs based on flapping tails and fins are the most advantageous choice for insect-scale AUV propulsion.

The research presented in this paper was partially funded by the Washington State University (WSU) Foundation and the Palouse Club through a Cougar Cage Award to N.O.P.-A.; the US National Science Foundation (NSF) through Award 2244082; the Morgan Family Charitable Trust through a direct gift to N.O.P.-A.; and, the Koerner Family Foundation (KFF) through a graduate fellowship to C.K.T. Additional funding was provided by the WSU Voiland College of Engineering and Architecture through a start-up fund to N.O.P.-A..

The authors are with the School of Mechanical and Materials Engineering, Washington State University (WSU), Pullman, WA 99164, USA. Corresponding authors' e-mail: conor.trygstad@wsu.edu (C.K.T.); n.perezarancibia@wsu.edu (N.O.P.-A.).

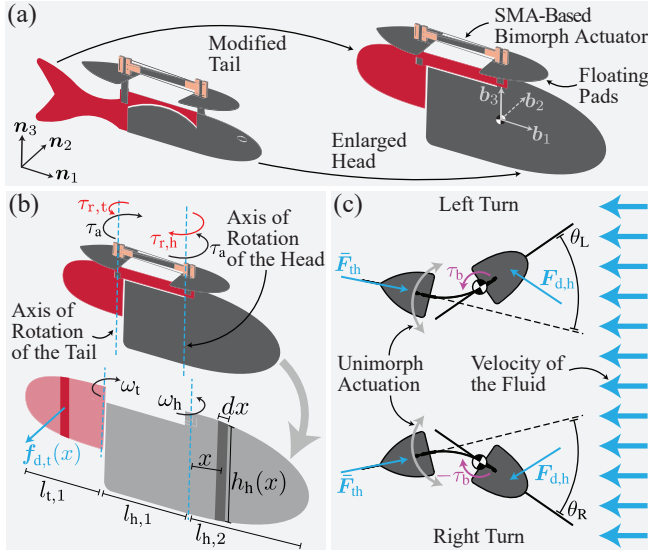


Fig. 1. An evolved version of the FRISSHBot platform. A prototype of the original design presented in [1] is shown on the left, and a prototype of the new design on the right. A 28-mm-long paper clip was included in the photograph to indicate scale.

Over the past few years, we have developed several mm-scale aquatic robots that employ undulating soft tails to generate the propulsive forces required for swimming by leveraging fluid–structure interaction [1]–[3]. The most notable of these prototypes is the VLEIBot<sup>++</sup> presented in [3], a 900-mg autonomous swimmer that uses the dual-tail design introduced in [2] for generating thrust and achieving *two-dimensional* (2D) tracking control. Nevertheless, considering the vast biological evidence available, we hypothesize that single-tail designs can potentially achieve higher swimming performance and efficiency; furthermore, single-tail robots can be designed to have relatively small cross-sectional areas, thus enabling high accessibility to confined spaces and maneuverability. These observations prompted us to develop the 10-mg *shape-memory alloy* (SMA)-based bimorph actuator presented in [1], which is the key element that enabled the creation of the original single-tail *Fish-&-Ribbon-Inspired Small Swimming Harmonic roBot* (FRISSHBot), shown on the left in Fig. 1.

Despite being the smallest robotic swimmer with onboard actuation developed at the time of publication, the swimming performance of the original FRISSHBot platform was sub-optimal and steerability was not achieved. In this paper, we present an evolved controllable version of this swimmer—shown on the right in Fig. 1. This new platform features modified head and tail designs, which were developed through basic fluid-mechanics analyses and collection of empirical data. The resulting swimmer has a mass of 59 mg, is 36 mm long, and achieves average swimming speeds on the order of 13.6 mm/s (0.38 BI/s), which is over four times faster than the original prototype. As discussed in Section IV, this new platform is highly maneuverable and controllable in the 2D space. Prior to this instance, only the subgram swimmer presented in [2] has been demonstrated to operate in closed loop, employing onboard actuation.

Here, we present closed-loop trajectory-tracking experiments in which the tested FRISSHBot prototype achieved control errors with *root-mean-square* (RMS) values as low as 2.6 mm during rectilinear locomotion—an improvement of



**Fig. 2. Design and functionality of the new FRISSHBot platform.** The vector triplets  $\{n_1, n_2, n_3\}$  and  $\{b_1, b_2, b_3\}$  define the inertial and body-fixed frames used for kinematic and kinetic analyses. (a) Design evolution of the FRISSHBot platform. As seen, the planform of the tail was modified from a caudal to a parabolic shape, and the planform of the head was enlarged. (b) Idealized dynamical model of the new FRISSHBot platform. During swimming, the robot's actuator generates two torques with equal instantaneous signed magnitudes,  $\tau_a(t)$ , and opposite directions along the  $b_3$  axis. The periodic oscillation of the swimmer generates resistive hydrodynamic torques acting on the head and tail; the signed magnitudes of these torques are labeled as  $\tau_{r,h}$  and  $\tau_{r,t}$ , respectively. (c) Turning during swimming is achieved by operating the robot's actuator in a unimorph mode—left or right. A left turn is generated by the aggregation of two torques with direction  $b_3$ —one tail-induced and the other head-induced. Similarly, a right turn is generated by the aggregation of two torques with direction  $-b_3$ —one tail-induced and the other head-induced.

35% with respect to that achieved by the dual-tail VLEIBot<sup>+</sup> platform presented in [2]. During closed-loop left-turn and right-turn tracking experiments, the tested swimmer achieved turning rates of up to 13.1°/s, which is comparable to the rates reported for the VLEIBot<sup>+</sup> in [2]. Notably, the measured turning radii during these tests are as small as 10 mm (0.28 BI), which is about 88% lower than that measured for the VLEIBot<sup>+</sup>. These new results provide empirical evidence suggesting that a higher swimming maneuverability can be attained using a single-tail propulsor in comparison to that achievable with dual-tail designs. To the best of our knowledge, this is the first demonstration of feedback-controlled swimming tests employing a single-tail subgram platform reported to date.

The rest of the paper is organized as follows. Section II presents the physics-based design and functionality of the new FRISSHBot platform. Section III describes the experiments performed to characterize the peak-to-peak lateral excursion of the swimmer's tail during actuation, and presents an analysis of the measured forward speeds and turning rates across its range of operation. Section IV presents feedback-controlled trajectory-tracking swimming tests using the new FRISSHBot platform and discusses the achieved performance in terms of tracking errors. Last, Section V summarizes the research presented in the paper and discusses directions for future work.

## II. DESIGN OF THE NEW FRISSHBOT

In this section, we present the design and discuss the functionality of the new FRISSHBot platform. As seen in Fig. 2(a), we evolved the design of the original swimmer presented in [1] to increase locomotion performance and achieve empirical 2D controllability. The two main modi-

fications are an enlarged head and a new propulsive tail, which we varied from a caudal to a parabolic planform. It is a well-established empirical fact that, for an underwater propulsive flapping foil operating at low Reynolds numbers, greater stroke amplitudes and frequencies typically generate higher thrust forces [30], [31]. Prompted by this physical fact, we aimed to generate a design that increases the stroke amplitude of the swimmer's tail compared to that of the original robot—which we use as a benchmark—at the same frequency of actuation. For analysis and development purposes, we use the dynamical model in Fig. 2(b). As seen here, a FRISSHBot prototype is mechanically powered by a bimorph SMA-based actuator of the type introduced in [1].

To describe the kinematics and kinetics of the system, we use the laboratory-fixed inertial and body-fixed frames of reference defined by the vector triplets  $\{n_1, n_2, n_3\}$  and  $\{b_1, b_2, b_3\}$ , respectively; the origin of the body-fixed frame coincides with the *center of mass* (CoM) of the robot. According to the model in Fig. 2(b), during swimming, the actuator generates two torques with equal instantaneous signed magnitudes,  $\tau_a(t)$ , and opposite directions along the  $b_3$  axis. Note that, as defined,  $\tau_a(t) > 0$  when the corresponding vector,  $\tau_a(t)$ , acting on the head points in the direction of  $b_3$ . Consistent with this convention and the graphically defined vectors in Fig. 2(b), the instantaneous signed angular speed of the head,  $\omega_h(t)$ , is positive when the direction of its corresponding angular velocity,  $\omega_h(t)$ , points in the direction of  $b_3$ ; similarly, the instantaneous signed angular speed of the tail,  $\omega_t(t)$ , is positive when the direction of its corresponding angular velocity,  $\omega_t(t)$ , points in the direction of  $-b_3$ . As described in [1], the bimorph actuator driving the swimmer can be thought of as being composed of two SMA-based subsystems—left and right. When both sides are actuated alternately, we say that the actuator functions in the bimorph mode; when only one side is actuated, we say that the actuator functions in a unimorph mode—left or right. In the bimorph mode, the swimmer oscillates by cyclically bending to the left and right, while, by design, its head functions as an anchor and its tail as a propulsor.

By mathematically describing the head and tail of the robot as plates, we can model the aggregated viscous and inertial reactions of the surrounding water acting on the swimmer as two reactive torques: one corresponding to the head, with signed magnitude  $\tau_{r,h}$ , which is positive when the direction of its corresponding vector,  $\tau_{r,h}$ , points in the direction of  $-b_3$ ; and, another corresponding to the tail, with signed magnitude  $\tau_{r,t}$ , which is positive when the direction of its corresponding vector,  $\tau_{r,t}$ , points in the direction of  $b_3$ . Thus, noting that in this case all the torques are applied along the direction of  $b_3$  or  $-b_3$ , the instantaneous total torque acting on the robot during swimming,  $\tau_b(t) = \tau_b(t) \cdot b_3$ , can be described with the scalar equation

$$\begin{aligned} \tau_b(t) &= \tau_h(t) + \tau_t(t) \\ &= [\tau_a(t) + \tau_{r,h}(t)] + [-\tau_a(t) + \tau_{r,t}(t)] \\ &= -\tau_{r,h}(t) + \tau_{r,t}(t), \end{aligned} \quad (1)$$

where  $\tau_h(t)$  and  $\tau_t(t)$  are the instantaneous signed magnitudes of the total torques acting on the head and tail, respectively. Since the robot is assumed to swim rectilinearly, its net time-average rotation, with respect to the inertial frame, after an actuation cycle must be zero. Thus, from Euler's second law,

$$\langle \tau_b(t) \rangle = \langle -\tau_{r,h}(t) + \tau_{r,t}(t) \rangle = -\langle \tau_{r,h}(t) \rangle + \langle \tau_{r,t}(t) \rangle = 0, \quad (2)$$

from which it follows that

$$\langle \tau_{r,h}(t) \rangle = \langle \tau_{r,t}(t) \rangle. \quad (3)$$

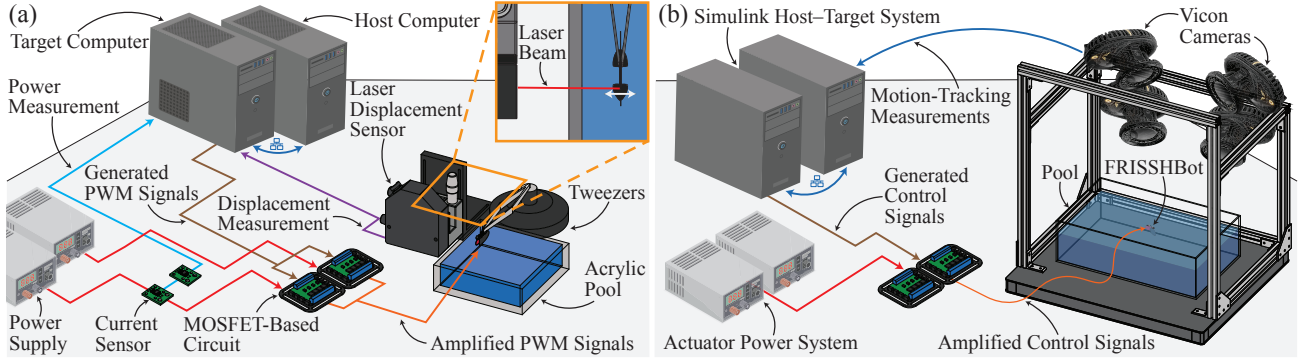


Fig. 3. **Experimental characterization of the new FRISSHBot platform.** (a) Setup used to measure the lateral excursion of the swimmer’s tail and power consumption of the driving actuator during constrained operation. In this setup, signals are generated, monitored, and recorded using a Mathworks Simulink Real-Time host–target system equipped with a PCI-6229 AD/DA board. The two PWM voltages used to excite the bimorph actuator of the tested prototype are generated following the method described in [1]. (b) Setup used to perform swimming experiments with the tested FRISSHBot prototype. The host–target system in (a) is used for signal generation, monitoring, data collection, and control. A Vicon motion-capture system with four VK16 cameras measures and records the position and orientation of the robot in space, which is required for closed-loop control implementation.

For each of the two plates, using the method in [32], we can compute the magnitude of the corresponding total reactive torque as

$$\begin{aligned} \tau_{r,p}(t) &= \int_{-l_{p,1}}^{l_{p,2}} f_{d,p}(x) x dx \\ &= -\frac{1}{2} \rho C_d \omega_p(t) |\omega_p(t)| \int_{-l_{p,1}}^{l_{p,2}} h_p(x) |x|^3 dx, \end{aligned} \quad (4)$$

in which  $p \in \{h, t\}$ ;  $-l_{p,1} \leq 0$  and  $l_{p,2} \geq 0$  are the lateral limits of the plate, measured from the axis of rotation;  $f_{d,p}(x) = -\frac{1}{2} \rho C_d h_p(x) \omega_p(t) |\omega_p(t)| x |x|$  is the signed magnitude of the drag force per unit length along the span of the plate at a distance  $x$  from the axis of rotation;  $\rho$  is the density of water;  $C_d$  is a dimensionless drag coefficient;  $\omega_p(t)$  is the instantaneous signed angular speed at which the plate rotates about its axis of rotation; and,  $h_p(x)$  is the plate chord at position  $x$ . Thus, substituting (4) into (3), we obtain that, during rectilinear swimming,

$$\langle \omega_h^2(t) \rangle \int_{-l_{h,1}}^{l_{h,2}} h_h(x) |x|^3 dx = \langle \omega_t^2(t) \rangle \int_{-l_{t,1}}^{l_{t,2}} h_t(x) |x|^3 dx, \quad (5)$$

in which  $I_h = \int_{-l_{h,1}}^{l_{h,2}} h_h(x) |x|^3 dx$ ,  $I_t = \int_{-l_{t,1}}^{l_{t,2}} h_t(x) |x|^3 dx$  are *resistive drag factors* (RDFs). Note that in the derivation of the expression specified by (5), we used the fact that, in agreement with the graphical definitions in Fig. 2(b) and the dynamics of the FRISSHBot, at any given instant, the signs of  $\omega_h(t)$  and  $\omega_t(t)$  are the same.

The expression specified by (5) can be used directly as a guideline for design: specifically, to maximize the angular speed of the tail during swimming—such that it functions as a propulsor—and minimize the angular speed of the head—such that it functions as an anchor. This expression indicates that a simple approach to increase the value of  $I_h$ , relative to that of  $I_t$ , is to make the head taller and longer than the tail. In the design of the original FRISSHBot platform, the head and tail have similar average heights, i.e.,  $\bar{h}_h \approx \bar{h}_t$ . Additionally, the tail of that platform was designed with most of its area located far away from its axis of rotation, which resulted in a relatively high  $I_t$  value and corresponding reactive torque, thus limiting the tail’s mobility relative to the head and surrounding water. We hypothesize that this lack of mobility severely degrades the swimming performance of that robot. As shown in Figs. 2(a) and (b), in the design of the new FRISSHBot, the head is significantly taller along the vertical dimension than

the tail, which is shorter along the longitudinal dimension than in the original robot, thereby placing the tail’s center of area closer to its axis of rotation. Together, these two design modifications resulted in a significantly larger reactive torque acting on the head than on the tail. We determined the final dimensions of the robotic design—particularly those of the head and tail—using a heuristic process based on open-loop straight-swimming and turning experiments, with the goal of maximizing speed and maneuverability. The resulting values for the RDFs of the new design are  $I_h = 1.14 \times 10^5 \text{ mm}^5$  and  $I_t = 1.07 \times 10^4 \text{ mm}^5$ . The values for the RDFs of the old design are  $I_h = 1.88 \times 10^4 \text{ mm}^5$  and  $I_t = 2.19 \times 10^4 \text{ mm}^5$ . Thus, through the design process, we modified the robot such that  $I_h : 1.88 \times 10^4 \text{ mm}^5 \rightarrow 1.14 \times 10^5 \text{ mm}^5$  and  $I_t : 2.19 \times 10^4 \text{ mm}^5 \rightarrow 1.07 \times 10^4 \text{ mm}^5$ .

Once more employing (5) for basic dynamical analysis, it can be determined that the enhanced design shown in Figs. 2(a) and (b) not only increases the swimming performance in terms of steady-state speed, but also improves the performance and reliability of turning, thereby enabling full 2D controllability. An explanation of the turning mechanism and steering strategy is depicted in Fig. 2(c). As seen here, to perform a turn, the actuator of the swimmer is operated in one of the two unimorph modes, as described in [1]. When operated in a unimorph mode, the robot periodically bends asymmetrically with a bias in the direction of actuation. Namely, when the left SMA-based subsystem of the actuator is excited and the right subsystem is kept inactive, the robot arcs periodically with its distal ends toward the left and its point of maximum convexity toward the right. Thus, during each actuation cycle, the lateral excursion of the tail relative to the longitudinal axis of the head is biased toward the left, which is denoted as  $\theta_L$  in Fig. 2(c). Analogously, when the right SMA-based subsystem of the actuator is excited and the left subsystem is kept inactive, the robot arcs periodically with its distal ends toward the right and its point of maximum convexity toward the left. As a consequence, during each actuation cycle, the lateral excursion of the tail relative to the longitudinal axis of the head is biased toward the right, which is denoted as  $\theta_R$  in Fig. 2(c).

During a left turn, the biased periodic bending of the swimmer forces the average thrust vector produced by the tail,  $\bar{F}_{th}$ , to act at an angle  $\theta_L$  (see the upper illustration in Fig. 2(c)) with respect to the longitudinal axis of the head. By design, this vector also acts at a distance from the robot’s CoM, thus creating a tail-induced left-turning torque (about  $b_3$ ) and, as a result, a left turn. Additionally, since, immediately prior to initiating a turn, the robot is swimming forward

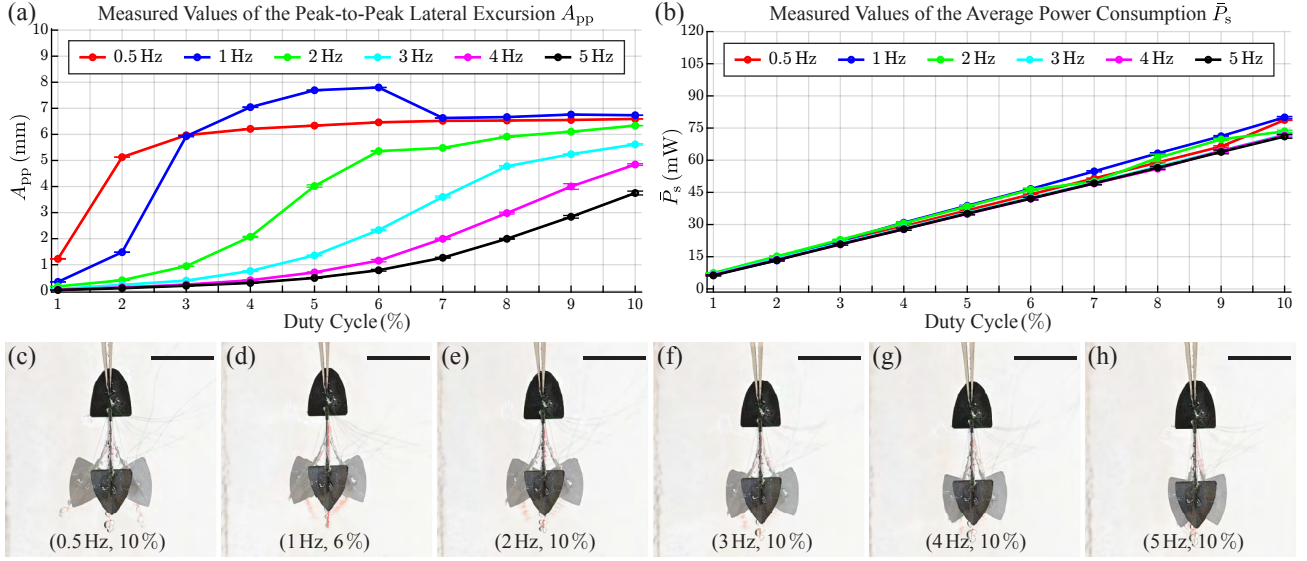


Fig. 4. **Peak-to-peak lateral excursion and average power consumption.** (a) Each data point corresponds to the mean—and associated ESD—of the measured peak-to-peak lateral excursions,  $A_{pp}$ , in 30 s of steady-state data. In this case, each ESD value represents the cycle-to-cycle variation of the excursion measurements for the corresponding experiment. (b) Each data point corresponds to the mean—and associated ESD—of the average power consumption,  $\bar{P}_s$ , from 30 s of steady-state data. In this case, each ESD value represents the cycle-to-cycle variation of the average power consumption. (c)–(h) Composites of video frames taken at the instants of maximum stroke displacements (left and right), and at rest for PWM excitations with frequencies of 0.5, 1, 2, 3, 4, and 5 Hz, while operating at their respective DC values of maximum lateral excursion. The scale bars in the images indicate a length of 10 mm. Video footage of these experiments is shown in the accompanying supplementary movie.

in the direction of  $\mathbf{b}_1$ , the tail-induced left turn generates an additional hydrodynamic drag force,  $\mathbf{F}_{d,h}$ —with inertial and viscous components—that, in turn, produces a head-induced left-turning torque (about  $\mathbf{b}_3$ ), which increases the rate of left rotation. During a right turn, the biased periodic bending of the swimmer forces the average thrust produced by the tail,  $\bar{\mathbf{F}}_{th}$ , to act at an angle  $\theta_R$  (see the lower illustration in Fig. 2(c)) with respect to the longitudinal axis of the head. By design, this thrust also acts at a distance from the robot’s CoM, thus creating a tail-induced right-turning torque (about  $-\mathbf{b}_3$ ) and, as a result, a right turn. Furthermore, analogous to the left-turning case, a tail-induced right turn induces an additional hydrodynamic drag force,  $\mathbf{F}_{d,h}$ —with inertial and viscous components—that, in turn, generates a head-induced right-turning torque (about  $-\mathbf{b}_3$ ), which increases the rate of right rotation.

In summary, a left turn is generated by the aggregation of two torques with direction  $\mathbf{b}_3$ —one tail-induced and the other head-induced. Similarly, a right turn is generated by the aggregation of two torques with direction  $-\mathbf{b}_3$ —one tail-induced and the other head-induced. By leveraging the enhanced capabilities of the new FRISSHBot design, we demonstrate that 2D controllability can be achieved through a combination of unimorph and bimorph actuation modes.

### III. CHARACTERIZATION OF THE NEW FRISSHBOT

#### A. Metrics of Swimming Efficiency

Two common metrics employed to compare the efficiency of swimming robots are the *cost of transport* (CoT) and *Strouhal number* (St), defined as

$$\text{CoT} = \frac{\bar{P}_s}{mg\bar{v}} \quad \text{and} \quad \text{St} = \frac{f_o A_{pp}}{\bar{v}}, \quad (6)$$

in which  $\bar{P}_s$  is the average power consumed by the swimmer during operation;  $m$  is the total mass of the swimmer;  $g$  is the acceleration of gravity;  $\bar{v}$  is the average speed of the swimmer in steady state, relative to the surrounding water;  $f_o$  is the frequency at which the swimmer’s tail is oscillated during operation; and,  $A_{pp}$  is the peak-to-peak

lateral excursion—left to right or vice versa, as shown in Fig. 2(b)—of the tail at its free distal end. Recently, however, another metric of swimming efficiency—the *swim number* (Sw) [33]—has been proposed because it provides a unified scaling law across all swimming modes and size scales. Namely,

$$\text{Sw} = 2\pi \cdot \text{Re} \cdot \text{St} = 2\pi \cdot \frac{\bar{v}L}{\nu} \cdot \frac{f_o A_{pp}}{\bar{v}} = \frac{2\pi f_o A_{pp} L}{\nu}, \quad (7)$$

in which Re is the Reynolds number;  $L$  is the length of the swimmer; and,  $\nu$  is the kinematic viscosity of water.

Directly from its definition, it follows that the CoT quantifies the energy required to move a unit of weight over a unit of distance, which implies that this parameter obeys different scaling laws across swim modes and size scales. Along the same lines, directly from its definition, it follows that the St—by relating tail-beat frequency, amplitude, and forward speed—provides insight into propulsion efficiency and flow regime. A limitation of this definition is that the St value quantifies swimming performance using only one length scale, which limits its ability to reflect the complex, multi-scale nature of real swimming systems—especially when comparing across swim modes or size scales. In contrast, the Sw accounts for both relevant length scales—oscillation amplitude and body length—as well as the fluid properties. To experimentally quantify the CoT, St, and Sw, we measured the values of  $\bar{P}_s$ ,  $\bar{v}$ , and  $A_{pp}$  across a range of *pulse-width modulation* (PWM) excitation signals, using the experimental setups discussed next.

#### B. Experimental Setups

We use the experimental setup depicted in Fig. 3(a) to measure the lateral excursion of the tail and power consumed by the tested FRISSHBot prototype during constrained operation (see the inset on the upper-right). In this setup, signals are generated, monitored, and recorded using a Mathworks Simulink Real-Time host–target system equipped with a PCI-6229 AD/DA board. The two PWM voltages used to excite the bimorph actuator of the tested swimmer are generated employing the method described in [1]. Accordingly,

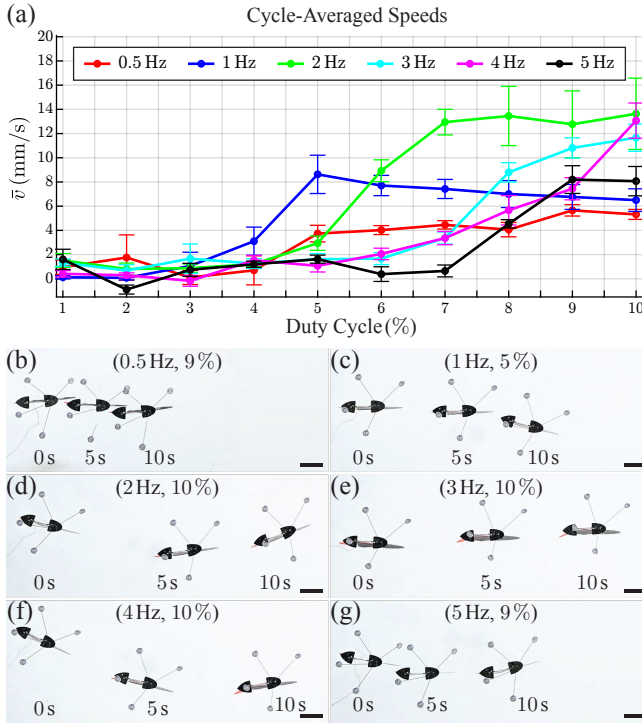


Fig. 5. **Average speed values recorded during open-loop swimming tests.** (a) Each data point corresponds to the mean—and associated ESD—of the cycle-averaged swimming speeds measured from 10 s of steady-state data. In this case, each ESD value represents the cycle-to-cycle variation of the average speed measurements. (b)–(g) Composites of frames taken at 5-s intervals from overhead video footage of the FRISSHBot prototype swimming at its maximum recorded speed for each tested frequency reported in (a). The scale bars in the images indicate a length of 10 mm. Video footage of these experiments is shown in the accompanying supplementary movie.

both exciting signals have the same frequency,  $f$ —which in this case coincides with  $f_0$ —and the same on-height, but their phases are shifted by  $180^\circ$ . To supply the power consumed by the two SMA-based subsystems of the actuator, we use two MOSFET-based switching circuits (four-channel YYNMOS-4). During symmetric bimorph actuation, the duty cycle (DC) of both exciting PWM signals is identical; during unimorph actuation, as explained in Section II, one side of the actuator is excited while the other side is left inactive (DC = 0). A diverse set of mixed actuation modes—created by sequentially combining bimorph and unimorph modes—can be generated by varying the DC values of the PWM signals exciting both sides of the driving actuator. As seen on the bottom-left of the illustration in Fig. 3(a), two current sensors (Pololu 05AU)—connected in series with the power supplies that feed the MOSFET-based circuits—are used to measure the instantaneous currents flowing through each side of the actuator during operation. Similarly to the cases discussed in [17], [34], and [35], during the tests, we measure the instantaneous displacement of the actuator at the connection point with the robot’s tail using a laser displacement sensor (Keyence LK-031). All the signals used for system characterization are generated and recorded at a sample-and-hold rate of 10 kHz.

Before conducting the experimental characterization of the lateral excursion of the robot’s tail and power consumption of the actuator during operation, we connected five 52-AWG tether wires in parallel to each terminal on both sides of the bimorph actuator. This electrical connection was heuristically selected to minimize power dissipation while maintaining sufficient flexibility to avoid any impediment to the function-

ality of the actuator. In addition, we prepared a swimming environment for the robot by filling a small acrylic pool with distilled water. During these experiments, the head of the tested FRISSHBot prototype is held immobile using a pair of tweezers, in the same position relative to the water surface as during swimming—i.e., with the floating pads in contact with the surface—as shown in the inset of Fig. 3(a). For a consistent basis of comparison and analysis, we heuristically set the on-height voltage of the exciting PWM signals such that a nominal current of 250 mA flows through each side of the actuator; in this case, the required on-height voltage is approximately 4 V. For the lateral excursion characterization, we excited the bimorph actuator of the tested prototype using all the PWM signals corresponding to the  $f$ -DC pairs with values in the sets  $f \in \{0.5, 1, 2, 3, 4, 5\}$  Hz and  $DC \in \{1:1:10\}\%$ . For each data set corresponding to a tested PWM excitation, we computed the mean of the measured peak-to-peak tail lateral excursions and mean of the robot’s cyclic-averaged power consumptions from 30 s of steady-state data. Additionally, for each mean value, we computed the corresponding *experimental standard deviation* (ESD), which quantifies the cycle-to-cycle variation in lateral excursion of the tail and average power consumption of the robot. Note that by immobilizing the head of the swimmer during the tests, we maximize the peak-to-peak lateral excursion of the tail; thus, the estimates of the  $St$  and  $Sw$ —presented in Section III-C—should be considered to be upper bounds.

To assess the swimming speed and turning performance of the tested FRISSHBot prototype, we used the experimental setup depicted in Fig. 3(b), in which the same host–target and power-electronics systems in Fig. 3(a) are used to drive the bimorph actuator of the swimmer. During these swimming tests, a Vicon motion-capture system with four VK16 cameras measures and records the position and orientation of the robot in space. These data are streamed, employing Tracker 10.0, to the host–target system at a rate of 250 Hz for monitoring, feedback control, and collection. Before performing a swimming experiment, we install retroreflective markers on the tested swimmer for motion tracking and place the robot in a pool filled with distilled water. For assessing open-loop forward swimming, we used the same set of exciting PWM signals as in the lateral-excision experiments discussed above. During open-loop turning experiments—performed using the strategy described in Section II and shown in Fig. 2(c)—we observed that PWM excitations with frequencies below 1 Hz or DC values below 5% do not produce noticeable turning. Therefore, we only tested unimorph actuation for turning—in both directions—using PWM excitations defined by the  $f$ -DC pairs with values in the sets  $f \in \{1, 2, 3, 4, 5\}$  Hz and  $DC \in \{5:1:15\}\%$ . For each tested combination of PWM voltages, we estimated the average signed speed of the tested FRISSHBot prototype—along the  $b_1$  axis—and average signed turning rate—about the  $b_3$  axis—from 10 s of steady-state experimental data. The results for these experiments are discussed next.

### C. Results and Discussion

Fig. 4(a) summarizes the experimental data obtained from the tests conducted to measure the peak-to-peak lateral excursion,  $A_{pp}$ , of the flapping tail for the selected set of PWM excitations (see Section III-B). Fig. 4(b) summarizes the data on the average power consumption corresponding to the same experiments. In the plot of Fig. 4(a), each data point shows the mean value and corresponding ESD of the measured cyclic  $A_{pp}$  values in 30 s of steady-state data. As observed, the peak-to-peak lateral excursion increases with the DC value. At an actuation frequency of 1 Hz, the average of the lateral excursion reaches its maximum of

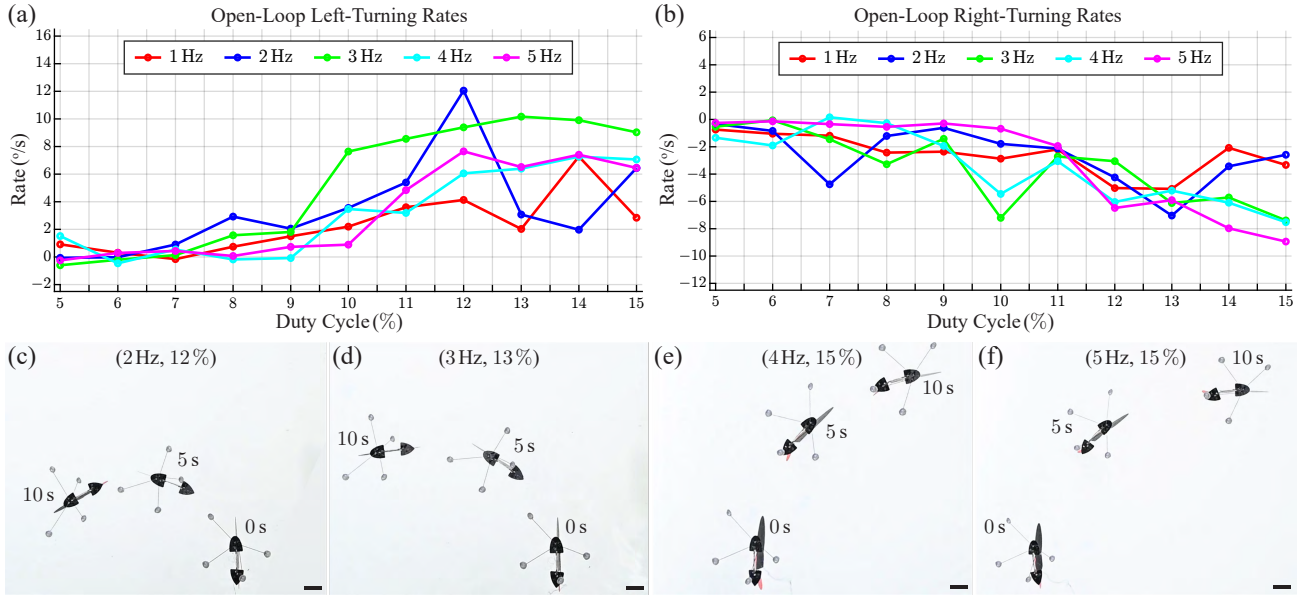


Fig. 6. **Open-loop turning maneuvers.** (a)–(b) Each data point indicates the average signed turning rate (relative to  $\mathbf{b}_3$ ) recorded during a turning maneuver, computed from 10 s of steady-state data. (c)–(f) Composites of frames taken at 5-s intervals from overhead video footage of the FRISSHBot prototype performing turns at its maximum recorded turning rate as reported in (a) and (b). The scale bars in the images indicate a length of 10 mm. Video footage of these experiments is shown in the accompanying supplementary movie.

7.80 mm at a DC of 6%, then slightly decreases at higher DC values. Maximum averages of 6.59, 6.34, 5.62, 4.84, and 3.75 mm at a DC of 10% were measured for frequencies of 0.5, 2, 3, 4, and 5 Hz, respectively. Photographic composites of the peak-to-peak lateral excursions recorded during these six tests are presented in Figs. 4(c)–(h). As seen in these images, the resulting stroke envelopes remain approximately symmetric up to the frequency of 4 Hz; at 5 Hz, the lateral excursion becomes biased toward the right side. As expected, Fig. 4(b) indicates that the mean of the average power consumption increases approximately linearly with the DC value and is mostly independent of the actuation frequency. For a frequency of 5 Hz, this relationship can be approximated as  $\bar{P}_s(\text{DC}) = 720 \cdot \text{DC}$  [mW], with the DC value in per unit.

Fig. 5(a) summarizes the data obtained from 60 open-loop forward-swimming tests. In this plot, each data point shows the mean of the measured cycle-averaged forward speeds in 10 s of steady-state data and the corresponding ESD. Generally, these results indicate a positive correlation between average steady-state speed and DC for most tested frequencies. Photographic composites of frames, taken at 5-s intervals, show the tested FRISSHBot prototype swimming at its peak speed for each experimental frequency in Figs. 5(b)–(g). The recorded swimming speed with the largest mean of 13.6 mm/s corresponds to a DC value of 10% and a frequency of 2 Hz. Notably, the mean speeds corresponding to the same DC of 10%, for frequencies of 3 and 4 Hz, are comparable to the recorded experimental maximum—11.7 and 13.1 mm/s, respectively—while the largest mean values for 0.5, 1, and 5 Hz are significantly lower, which suggests that the best operating frequencies for achieving high swimming performance are in the range from 2 to 4 Hz. When swimming at its maximum capacity (2 Hz, 10%), the tested FRISSHBot prototype travels about 4.4 times faster than its prior version, as reported in [1], and achieves CoT, Sw, and St values of 9304, 2868, and 0.93, respectively. Overall, these values indicate a low efficiency of energy conversion and swimming, as evidenced by the St of 0.93, which is well outside the reported optimal range of 0.25 to 0.35 [36]. The lowest recorded St value of 0.57 for the tested

swimmer occurs when operating at 0.5 Hz with a DC of 9%. This St is much closer to the optimal range relative to that achieved at higher speeds; however, the corresponding CoT is 20127. These values indicate that with these excitation parameters, the swimmer is more efficient at transforming its flapping motion into locomotion but significantly more inefficient at transporting its mass, due to the relatively low forward swimming speed of 5.7 mm/s. Note, however, that this speed is still 1.9 times larger than that of the original FRISSHBot platform.

Figs. 6(a) and (b) summarize the experimental data obtained from open-loop left-turning (about  $\mathbf{b}_3$ ) and right-turning (about  $-\mathbf{b}_3$ ) experiments, respectively. Generally, the turning rate increases with the DC value for both directions—left and right. The two best left-turning cases, with average rates of 12.0 and 10.2  $^\circ/\text{s}$ , correspond to the  $f$ -DC pairs {2 Hz, 12%} and {3 Hz, 13%}, respectively. The two best right-turning cases, with average rates of 7.5 and 8.9  $^\circ/\text{s}$ , correspond to the  $f$ -DC pairs {4 Hz, 15%} and {5 Hz, 15%}, respectively. Photographic composites of frames, taken at 5-s intervals, of the left-turning and right-turning cases are presented in Figs. 6(c)–(f), respectively. Video footage of all the experiments discussed in this section is shown in the accompanying supplementary movie. Overall, the obtained experimental results provide preliminary but compelling evidence that single-tail swimmers of the FRISSHBot type represent a path toward achieving high swimming performance and efficiency at the subgram scale.

#### IV. FEEDBACK-CONTROLLED EXPERIMENTS

We performed feedback-controlled trajectory-tracking swimming experiments using the setup depicted in Fig. 3(b), already described above. The strategy and scheme for real-time control are shown in Figs. 7(a) and (b), which are presented in detail in [2] and [35]. As seen, the state of the system is given by the position of the robot's CoM relative to the origin of the inertial frame of reference,  $\mathbf{r} = [r_1 \ r_2]^T$ , and the heading,  $\psi$ , defined as the angle between  $\mathbf{b}_1$  and  $\mathbf{n}_1$ . As shown in Fig. 7(b), the control scheme is composed of two controllers: (i) a *lateral-position controller* (LPC); and, (ii) a

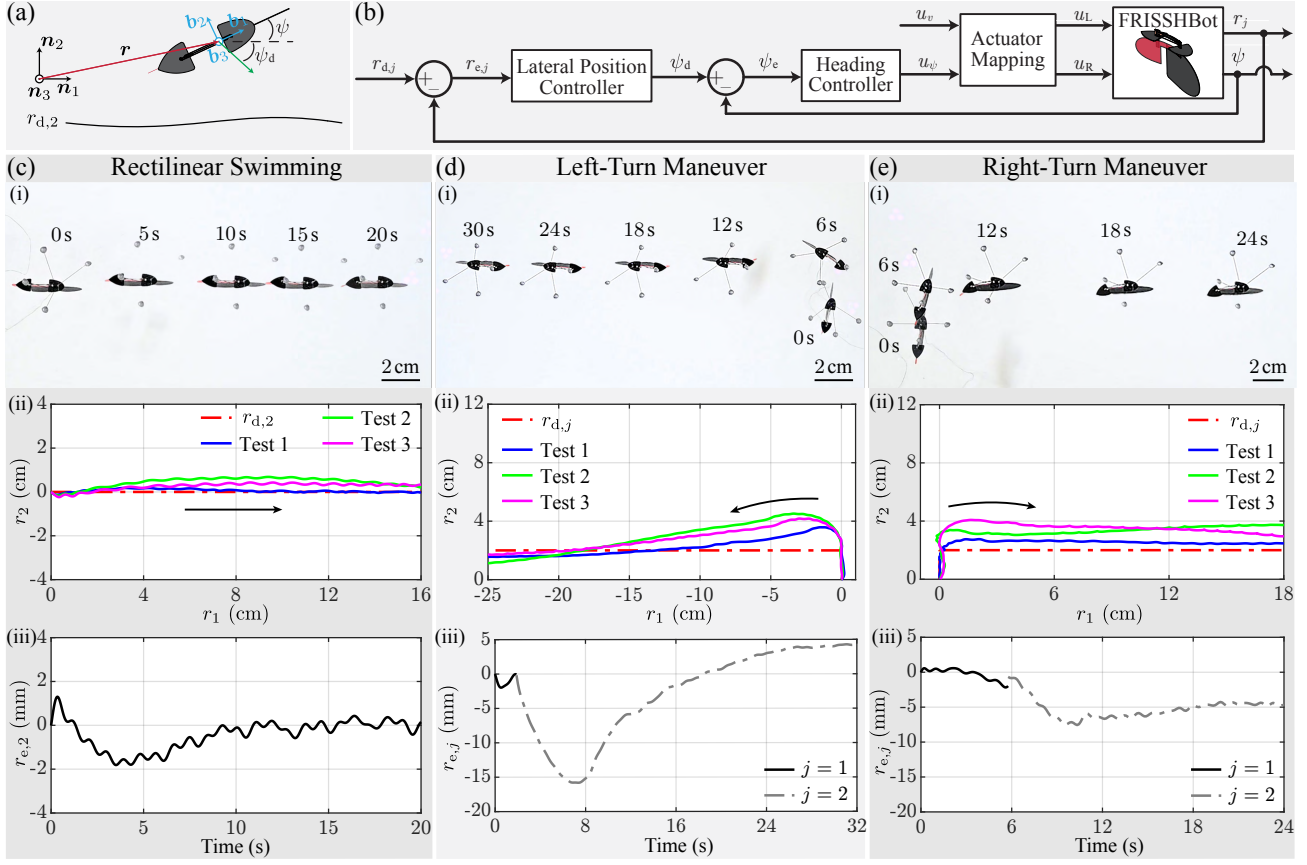


Fig. 7. **Feedback-controlled swimming experiments of the tested FRISSHBot prototype.** (a) Definition of the laboratory-fixed inertial and body-fixed frames of reference,  $\{n_1, n_2, n_3\}$  and  $\{b_1, b_2, b_3\}$ , respectively, and state of the system. Here,  $r$  is the position of the robot's CoM—which coincides with the origin of the body-fixed frame—relative to the origin of the inertial frame; and,  $\psi$  is the swimmer's heading. (b) Control scheme used during feedback trajectory-tracking swimming tests. (c) Feedback-controlled rectilinear swimming tests. (i) Composite of frames taken at 5-s intervals from video footage of rectilinear Test 1. (ii) Measured 2D trajectory of the swimmer following a straight-line reference path during Tests 1, 2, and 3. The arrow indicates the direction of motion. (iii) Lateral control error measured during Test 1. (d) Feedback-controlled left-turn tests. (i) Composite of frames taken at 6-s intervals from video footage of left-turn Test 1. (ii) Measured 2D trajectories of the swimmer during closed-loop left-turn Tests 1, 2, and 3. The arrow indicates the direction of motion. (iii) Lateral control error measured during Test 1. When the reference path is defined with respect to  $r_1$ , the control error is computed along that coordinate; consistently, when the reference path is defined with respect to  $r_2$ , the control error is computed along that coordinate. (e) Feedback-controlled right-turn tests. (i) Composite of frames taken at 6-s intervals from video footage of right-turn Test 1. (ii) Measured 2D trajectories of the swimmer during closed-loop right-turn Tests 1, 2, and 3. The arrow indicates the direction of motion. (iii) Lateral control error measured during Test 1. When the reference path is defined with respect to  $r_1$ , the control error is computed along that coordinate; consistently, when the reference path is defined with respect to  $r_2$ , the control error is computed along that coordinate. Video footage of these swimming experiments is shown in the accompanying supplementary movie.

*heading controller* (HC). The LPC receives as its input the lateral-position error,  $r_{e,j} = r_{d,j} - r_j$ , where  $r_{d,j}$  and  $r_j$  are the desired and measured lateral positions, respectively, with  $j = 1$  or 2, depending on the direction of the desired trajectory—horizontal or vertical. The desired heading,  $\psi_d$ , is computed by the LPC as

$$\psi_d(t) = k_p r_{e,j}(t) + k_i \int_0^t r_{e,j}(\tau) d\tau, \quad (8)$$

where  $k_p$  and  $k_i$  are proportional and integral controller gains. The HC receives as its input the heading error,  $\psi_e = \psi_d - \psi$ , and computes the heading input as  $u_\psi = k_{p,\psi} \psi_e$ , where  $k_{p,\psi}$  is a proportional gain. The actuator mapping receives as its inputs  $u_\psi$  and the open-loop speed reference,  $u_v$ , and maps them into DC values for the two PWM signals exciting the robot's bimorph actuator (see the rule presented in [35]).

For real-time implementation, based on the open-loop characterization results discussed in Section III, we selected the actuation frequency to be 3 Hz. The controller gains were empirically chosen to be  $k_p = 3$  rad/m,  $k_i = 1$  rad/(m · s), and  $k_{p,\psi} = 2$ /rad; and, the open-loop speed reference was set to  $u_v = 0.11$  per unit. In this manner, when the heading control error is zero, the two SMA-based subsystems of the

driving bimorph actuator are excited using PWM voltages with the same DC value of 11% (i.e.,  $u_R = u_L = 0.11$ ). When the heading control error is nonzero, the mapping adds  $u_\psi$  to the DC of the PWM signal exciting one side of the actuator and subtracts the same amount from the DC of the other side, as required to steer the robot in the direction that reduces the trajectory deviation. To avoid any potential actuator damage, we included a saturation law, such that  $u_R, u_L \leq 0.22$ , for all time. To assess the swimming performance and maneuverability of the tested robot, we conducted three back-to-back experiments for each of the following modes of operation: rectilinear swimming, right turning, and left turning. The data obtained from these tests are presented in Figs. 7(c)–(e). Here, Subfigures (i) show composites of video frames corresponding to the first test of each type (Test 1). The frames from the rectilinear swimming test were taken at intervals of 5 s; the frames from the turning experiments were taken at intervals of 6 s. Subfigures (ii) and (iii) show the reference and measured trajectories corresponding to Tests 1–3, and the lateral control error during Test 1, respectively. In the rectilinear-swimming cases, the tested swimmer achieved lateral control errors with RMS values on the order of 2.6 mm, and average

swimming speeds in excess of 9.1 mm/s. During the left-turn experiments, the tested swimmer achieved an average turning rate of 10.8°/s, an average turning radius on the order of 24 mm, and an average RMS value for the tracking error of about 10 mm. During the right-turn experiments, the tested swimmer achieved an average turning rate of 13.1°/s, an average turning radius on the order of 10 mm, and an average RMS value for the tracking error of about 11 mm. These experimental results clearly demonstrate the enhanced capabilities of the new FRISSHBot platform relative to those of the prior version reported in [1].

## V. CONCLUSION

We presented the new FRISSHBot—a 59-mg single-tail aquatic robot driven by an advanced 10-mg SMA-based bimorph actuator—which is an evolved 2D-controllable version of the swimmer first presented in [1]. This research was motivated by the goal of creating a bioinspired single-muscle mm-scale swimmer with full controllability and the capability of achieving high swimming performance. The resulting physics-informed design, developed using the notion of resistive drag factor, features an enlarged head and shortened tail relative to those of the original platform. The new swimmer was demonstrated to achieve average forward swimming speeds of up to 13.6 mm/s (0.38 Bl/s) when operating at 2 Hz, and high maneuverability—evidenced by the ability to turn at high angular speeds with small radii. During feedback-controlled trajectory-tracking swimming experiments, the tested prototype achieved control errors with RMS values as low as 2.6 mm. Along the same lines, the tested swimmer was demonstrated to turn with rates of up to 13.1°/s and turning radii as small as 10 mm. To the best of our knowledge, these are the first closed-loop swimming experiments implemented using a single-tail subgram aquatic robot reported to date. Through further design and development, we will continue evolving the current FRISSHBot platform to achieve power and control autonomy, high-efficiency energy conversion, high-performance swimming, and the ability to locomote underwater.

## REFERENCES

- [1] C. K. Trygstad, E. K. Blankenship, and N. O. Pérez-Arancibia, "A New 10-mg SMA-Based Fast Bimorph Actuator for Microrobotics," in *Proc. IEEE/RSJ Int. Conf. Intell. Robots Syst. (IROS)*, Abu Dhabi, UAE, Oct. 2024, pp. 1349–1356.
- [2] E. K. Blankenship, C. K. Trygstad, F. M. F. R. Gonçalves, and N. O. Pérez-Arancibia, "VLEIBot: A New 45-mg Swimming Microrobot Driven by a Bioinspired Anguilliform Propulsor," in *Proc. IEEE Int. Conf. Robot. Autom. (ICRA)*, Yokohama, Japan, May 2024, pp. 6014–6021.
- [3] C. R. Longwell, C. K. Trygstad, and N. O. Pérez-Arancibia, "Power-Efficient Actuation for Insect-Scale Autonomous Underwater Vehicles," in *Proc. Int. Symp. Robot. Res. (ISRR)*, Long Beach, CA, USA, Dec. 2024, Art. no. 39.
- [4] Q. Zhao, S. Liu, J. Chen, G. He, J. Di, L. Zhao, T. Su, M. Zhang, and Z. Hou, "Fast-moving piezoelectric micro-robotic fish with double caudal fins," *Robot. Auton. Syst.*, vol. 140, Jun. 2021, Art. no. 103733.
- [5] Z. Wang, G. Hang, J. Li, Y. Wang, and K. Xiao, "A micro-robot fish with embedded SMA wire actuated flexible biomimetic fin," *Sens. Actuators A: Phys.*, vol. 144, no. 2, pp. 354–360, Dec. 2008.
- [6] S. Guo, T. Fukuda, and K. Asaka, "A new type of fish-like underwater microrobot," *IEEE/ASME Trans. Mechatron.*, vol. 8, no. 1, pp. 136–141, Mar. 2003.
- [7] X. Deng and S. Avadhanula, "Biomimetic Micro Underwater Vehicle with Oscillating Fin Propulsion: System Design and Force Measurement," in *Proc. IEEE Int. Conf. Robot. Autom. (ICRA)*, Barcelona, Spain, Apr. 2005, pp. 3312–3317.
- [8] B. Kim, D.-H. Kim, J. Jung, and J.-O. Park, "A biomimetic undulatory tadpole robot using ionic polymer–metal composite actuators," *Smart Mater. Struct.*, vol. 14, no. 6, pp. 1579–1585, Dec. 2005.
- [9] Y. Chen, E. F. Helbling, N. Gravish, K. Ma, and R. J. Wood, "Hybrid aerial and aquatic locomotion in an at-scale robotic insect," in *Proc. IEEE/RSJ Int. Conf. Intell. Robots Syst. (IROS)*, Hamburg, Germany, Sep. 2015, pp. 331–338.
- [10] Y. Chen, H. Wang, E. F. Helbling, N. T. Jafferis, R. Zufferey, A. Ong, K. Ma, N. Gravish, P. Chirarattananon, M. Kovac, and R. J. Wood, "A biologically inspired, flapping-wing, hybrid aerial-aquatic microrobot," *Sci. Robot.*, vol. 2, no. 11, Oct. 2017, Art. no. ea05619.
- [11] P. Spino and D. Rus, "Towards Centimeter-Scale Underwater Mobile Robots: An Architecture for Capable  $\mu$ AUVs," in *Proc. IEEE Int. Conf. Robot. Autom. (ICRA)*, Yokohama, Japan, May 2024, pp. 1484–1490.
- [12] K. Li, X. Zhou, Y. Liu, J. Sun, X. Tian, H. Zheng, L. Zhang, J. Deng, J. Liu, W. Chen, and J. Zhao, "A 5 cm-Scale Piezoelectric Jetting Agile Underwater Robot," *Adv. Intell. Syst.*, vol. 5, no. 4, Apr. 2023, Art. no. 2200262.
- [13] D. Kim, M. Gwon, B. Kim, V. M. Ortega-Jimenez, S. Han, D. Kang, M. S. Bhamla, and J.-S. Koh, "Design of a Biologically Inspired Water-Walking Robot Powered by Artificial Muscle," *Micromachines*, vol. 13, no. 4, Apr. 2022, Art. no. 13040627.
- [14] O. Ozcan, H. Wang, J. D. Taylor, and M. Sitti, "STRIDE II: A Water Strider-inspired Miniature Robot with Circular Footpads," *Int. J. Adv. Robot. Syst.*, vol. 11, no. 6, Jun. 2014, Art. no. 85.
- [15] X. Zhang, J. Zhao, Q. Zhu, N. Chen, M. Zhang, and Q. Pan, "Bio-inspired Aquatic Microrobot Capable of Walking on Water Surface Like a Water Strider," *ACS Appl. Mater. Interfaces*, vol. 3, no. 7, pp. 2630–2636, Jul. 2011.
- [16] D. Zhao, R. Wang, S. Ding, J. Shan, X. Guan, Z. Li, J. Liang, W. Gu, B. Zhou, I. M. Lei, L. Lin, and J. Zhong, "Bio-Inspired Fast-Moving and Steerable Insect-Scale Soft Aquatic Surface Robot," *IEEE Trans. Robot.*, vol. 41, pp. 1825–1840, Feb. 2025.
- [17] C. K. Trygstad, X.-T. Nguyen, and N. O. Pérez-Arancibia, "A New 1-mg Fast Unimorph SMA-Based Actuator for Microrobotics," in *Proc. IEEE/RSJ Int. Conf. Intell. Robots Syst. (IROS)*, Detroit, MI, USA, Oct. 2023, pp. 2693–2700.
- [18] Y. S. Song and M. Sitti, "Surface-Tension-Driven Biologically Inspired Water Strider Robots: Theory and Experiments," *IEEE Trans. Robot.*, vol. 23, no. 3, pp. 578–589, Jun. 2007.
- [19] H. Gao, S. Jung, and E. F. Helbling, "High-speed interfacial flight of an insect-scale robot," in *Proc. IEEE Int. Conf. Robot. Autom. (ICRA)*, Yokohama, Japan, May 2024, pp. 6006–6013.
- [20] S. Zhou, W. Zhang, Y. Zou, X. Ke, F. Cui, and W. Liu, "Piezoelectric driven insect-inspired robot with flapping wings capable of skating on the water," *Electron. Lett.*, vol. 53, no. 9, pp. 579–580, Apr. 2017.
- [21] Q. Ze, S. Wu, J. Dai, S. Leanza, G. Ikeda, P. C. Yang, G. Iaccarino, and R. R. Zhao, "Spinning-enabled wireless amphibious origami millirobot," *Nat. Commun.*, vol. 13, Jun. 2022, Art. no. 3118.
- [22] J. Turner, M. Queen, and L. Assard, *Manual of Water Supply Practices—M28: Rehabilitation of Water Mains*, 3rd ed., American Water Works Association, Denver, CO, 2014.
- [23] F. Berlinger, M. Gauci, and R. Nagpal, "Implicit coordination for 3D underwater collective behaviors in a fish-inspired robot swarm," *Sci. Robot.*, vol. 6, no. 50, Jan. 2021, Art. no. eabd8668.
- [24] F. Berlinger, M. Duduta, H. Gloria, D. Clarke, R. Nagpal, and R. J. Wood, "A Modular Dielectric Elastomer Actuator to Drive Miniature Autonomous Underwater Vehicles," in *Proc. IEEE Int. Conf. Robot. Autom. (ICRA)*, Brisbane, Australia, May 2018, pp. 3429–3435.
- [25] J. Shintake, V. Cacciuolo, H. Shea, and D. Floreano, "Soft Biomimetic Fish Robot Made of Dielectric Elastomer Actuators," *Soft Robot.*, vol. 5, no. 4, pp. 466–474, Aug. 2018.
- [26] C. Rossi, J. Colorado, W. Coral, and A. Barrientos, "Bending continuous structures with SMAs: a novel robotic fish design," *Bioinsp. Biomim.*, vol. 6, no. 4, Dec. 2011, Art. no. 045005.
- [27] B. Bayat, A. Crespi, and A. Ijspeert, "Envirobot: A Bio-Inspired Environmental Monitoring Platform," in *Proc. IEEE/OES Auton. Underw. Veh. (AUV)*, Tokyo, Japan, Nov. 2016, pp. 381–386.
- [28] K. Struebig, B. Bayat, P. Eckert, A. Looijestijn, T. C. Lueth, and A. J. Ijspeert, "Design and development of the efficient anguilliform swimming robot—MAR," *Bioinsp. Biomim.*, vol. 15, no. 3, May 2020, Art. no. 035001.
- [29] D. M. Webber and R. K. O'Dor, "Monitoring the Metabolic Rate and Activity of Free-Swimming squid With Telemetered Jet Pressure," *J. Exp. Biol.*, vol. 126, no. 1, pp. 205–224, Nov. 1986.
- [30] H. Ding, R. Chen, Y. Zhu, H. Shen, and Q. Gao, "Effect of Frequency-Amplitude Parameter and Aspect Ratio on Propulsion Performance of Underwater Flapping-Foil," *Biomim.*, vol. 9, no. 6, Jun. 2024, Art. no. 324.
- [31] C. R. James, R. G. Sanelli, P. D. Spino, F. M. F. R. Gonçalves, C. K. Trygstad, N. O. Pérez-Arancibia, and K. I. Matveev, "A Novel Aquatic Propulsor Inspired by Mobiliform Swimming," in *Proc. Oceans*, Hampton Roads, VA, USA, Oct. 2022, Art. no. 9977324.
- [32] Y. Nakayama, *Introduction to Fluid Mechanics*, R. F. Boucher, Ed. Oxford, UK: Butterworth-Heinemann, 2000.
- [33] M. Coe and S. Gutschmidt, "Cost of Transport is not the whole story—A review," *Ocean Engin.*, vol. 313, Dec. 2024, Art. no. 119332.
- [34] X.-T. Nguyen, A. A. Calderón, A. Rigo, J. Z. Ge, and N. O. Pérez-Arancibia, "SMALLBug: A 30-mg Crawling Robot Driven by a High-Frequency Flexible SMA Microactuator," *IEEE Robot. Autom. Lett.*, vol. 5, no. 4, pp. 6796–6803, Oct. 2020.
- [35] R. M. Bena, X.-T. Nguyen, A. A. Calderón, A. Rigo, and N. O. Pérez-Arancibia, "SMART: A 60-mg Steerable Robot Driven by High-Frequency Shape-Memory Alloy Actuation," *IEEE Robot. Autom. Lett.*, vol. 6, no. 4, pp. 8173–8180, Oct. 2021.
- [36] G. K. Taylor, R. L. Nudds, and A. L. R. Thomas, "Flying and swimming animals cruise at a Strouhal number tuned for high power efficiency," *Nature*, vol. 425, pp. 707–711, Oct. 2003.